Computers and Mathematics with Applications 60 (2010) 1591–1606

Contents lists available at ScienceDirect

Computers and Mathematics with Applications

journal homepage: www.elsevier.com/locate/camwa

An unconditionally stable hybrid numerical method for solving the Allen–Cahn equation

Yibao Li, Hyun Geun Lee, Darae Jeong, Junseok Kim *

Department of Mathematics, Korea University, Seoul 136-701, Republic of Korea

ARTICLE INFO

Article history:
Received 4 November 2009
Received in revised form 13 May 2010
Accepted 24 June 2010

Keywords:
Allen–Cahn equation
Finite difference
Unconditionally stable
Operator splitting
Motion by mean curvature

ABSTRACT

We present an unconditionally stable second-order hybrid numerical method for solving the Allen–Cahn equation representing a model for antiphase domain coarsening in a binary mixture. The proposed method is based on operator splitting techniques. The Allen–Cahn equation was divided into a linear and a nonlinear equation. First, the linear equation was discretized using a Crank–Nicolson scheme and the resulting discrete system of equations was solved by a fast solver such as a multigrid method. The nonlinear equation was then solved analytically due to the availability of a closed-form solution. Various numerical experiments are presented to confirm the accuracy, efficiency, and stability of the proposed method. In particular, we show that the scheme is unconditionally stable and second-order accurate in both time and space.

1. Introduction

This paper presents an unconditionally stable second-order hybrid numerical method for solving the Allen–Cahn (AC) equation

$$\frac{\partial c(\mathbf{x},t)}{\partial t} = -M\left(\frac{F'(c(\mathbf{x},t))}{\epsilon^2} - \Delta c(\mathbf{x},t)\right), \quad \mathbf{x}\in\Omega,\ 0<t\le T, \tag{1}$$

where $\Omega \subset \mathbf{R}^d$ $(d = 1, 2, 3)$ is a domain [1]. The quantity $c(\mathbf{x}, t)$ is defined as the difference between the concentrations of the two components in a mixture. The coefficient, M, is a constant mobility and $M \equiv 1$ is taken for convenience. The function, $F(c) = 0.25(c^2 - 1)^2$, is the Helmholtz free energy density, as shown in Fig. 1 [2]. The small positive constant ϵ is the gradient energy coefficient related to the interfacial energy.

The boundary condition is

$$\frac{\partial c}{\partial \mathbf{n}} = 0 \quad \text{on } \partial\Omega, \tag{2}$$

where $\frac{\partial}{\partial \mathbf{n}}$ denotes the normal derivative on $\partial\Omega$. Let us define the Ginzburg–Landau free energy,

$$\mathcal{E}(c) := \int_\Omega \left(\frac{F(c)}{\epsilon^2} + \frac{|\nabla c|^2}{2}\right) d\mathbf{x}. \tag{3}$$

* Corresponding author.
E-mail address: cfdkim@korea.ac.kr (J. Kim).
URL: http://math.korea.ac.kr/~cfdkim/ (J. Kim).

0898-1221/$ – see front matter © 2010 Elsevier Ltd. All rights reserved.
doi:10.1016/j.camwa.2010.06.041

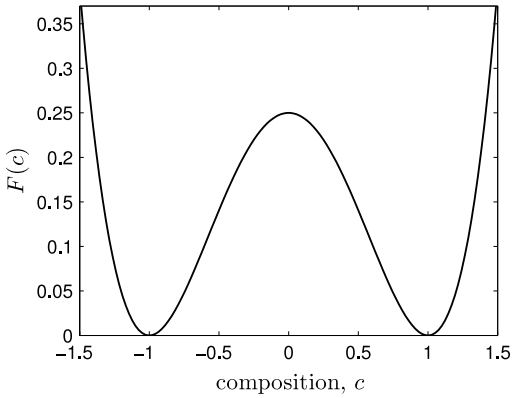

Fig. 1. A double-well potential, $F(c) = 0.25\ (c^2 - 1)^2$.

The AC equation can then be derived as the L^2-gradient flow of the total free energy, $\mathcal{E}(c)$ [3]. The AC equation was introduced originally as a phenomenological model for antiphase domain coarsening in a binary alloy [1]. The AC equation and its various modified forms have been applied in addressing a range of problems, such as those of phase transitions [1], image analysis [4,5], motion by mean curvature [6–11], two-phase fluid flows [12], and crystal growth [13,14]. Therefore, an efficient and accurate numerical solution of this equation is needed to better understand its dynamics.

In [4], the authors proposed the two-level semi-implicit finite-difference scheme. They observed that their scheme is dominated by the second-order difference operator. In [15], the authors proposed an unconditionally gradient stable scheme, which means that the discrete energy of Eq. (3) is decreasing regardless of time step size. Decreasing discrete energy implies the pointwise boundedness of the numerical solution for the AC equation. They showed that their scheme is indeed second-order accurate in space and first-order accurate in time. In [16], the authors proposed an adaptive finite-element approximation of the AC equation. In [17], the authors proposed a new numerical scheme that combines the adaptive moving mesh method with the semi-implicit Fourier spectral algorithm. Maintaining a similar accuracy, the proposed method was shown to be far more efficient than the existing methods for microstructures with small ratios of interfacial widths to the domain size. In [18], the authors used an adaptive mesh refinement with a second-order L_0-stable scheme. In [19], they used the exponential time differencing method [20]. Eyre reported that the AC equation becomes an unconditionally gradient stable algorithm if the free energy functional is split appropriately into contractive and expansive parts,

$$\begin{aligned}\mathcal{E}(c) &= \int_a^b \left(\frac{F(c)}{\epsilon^2} + \frac{c_x^2}{2}\right) \mathrm{d}x \\ &= \int_a^b \left(\frac{c^4+1}{4\epsilon^2} + \frac{c_x^2}{2}\right) \mathrm{d}x - \int_a^b \frac{c^2}{2\epsilon^2} \mathrm{d}x = \mathcal{E}_c(c) - \mathcal{E}_e(c), \end{aligned} \tag{4}$$

and the contractive part $\mathcal{E}_c(c)$ and expansive part $-\mathcal{E}_e(c)$ are treated implicitly and explicitly, respectively [21]. The nonlinearly stabilized splitting scheme that involves a semi-implicit time discretization and a centered difference space discretization of Eq. (1) is

$$\frac{c_i^{n+1} - c_i^n}{\Delta t} = \frac{c_i^n - (c_i^{n+1})^3}{\epsilon^2} + \Delta_h c_i^{n+1} \quad \text{for } i = 1, \ldots, N;\ n = 0, \ldots, N_t - 1, \tag{5}$$

where the discrete notation is defined in the following section. In [15], the authors reported the energy decreasing property for the corresponding discrete problem by using the eigenvalues of the Hessian matrix of the energy functional. An implicit Euler's scheme is

$$\frac{c_i^{n+1} - c_i^n}{\Delta t} = \frac{c_i^{n+1} - (c_i^{n+1})^3}{\epsilon^2} + \Delta_h c_i^{n+1}. \tag{6}$$

This scheme is much better than the simple explicit Euler's scheme. However, the implicit Euler's scheme suffers from instability if a large time step is used [22]. Eq. (5) can be reformulated as

$$\frac{c_i^{n+1} - c_i^n}{\frac{\Delta t \epsilon^2}{\Delta t + \epsilon^2}} = \frac{c_i^{n+1} - (c_i^{n+1})^3}{\epsilon^2} + \Delta_h c_i^{n+1}. \tag{7}$$

This suggests that the unconditionally gradient stable scheme can be considered a time step rescaling of the implicit Euler's scheme. In addition,

$$\Delta t_{\text{equiv}} = \frac{\Delta t \epsilon^2}{\Delta t + \epsilon^2} \leq \min(\Delta t, \epsilon^2). \tag{8}$$

That is, the scaled equivalent time step Δt_{equiv} is bounded by ϵ^2, which is a small value. In [23,24], the authors addressed unconditional stability of AC algorithms given by Eyre [22] and showed that the equivalent time step is bounded.

As Eyre noticed, the explicit Euler's scheme is not gradient stable and it was found that the stable time steps are severely restricted. The implicit Euler's scheme is conditionally gradient stable and it suffers from uniqueness problem of solution with large time steps. It turns out that the allowed time step sizes are just less than twice the explicit Euler's step. The Crank–Nicolson scheme also suffers from the solvability restriction. The semi-implicit Euler's scheme is much better compared to the explicit Euler's scheme, but still not gradient stable [22]. Eyre's scheme (Eq. (5)) also has the equivalent time step limitation. In this paper, we propose an unconditionally stable and accurate numerical method for solving the AC equation. The proposed method is based on operator splitting techniques. The AC equation was divided into a linear and a nonlinear equation. The linear equation was solved using a Crank–Nicolson scheme and the nonlinear equation was then solved analytically due to the availability of a closed-form solution. The main benefit of operator splitting methods is that the stability depends on the minimum of each term rather than the stability of all terms combined. The proposed scheme for the AC equation involves two steps. First, $c_t = \Delta c$ is solved numerically using a Crank–Nicolson method. Second, $c_t = (c - c^3)/\epsilon^2$ is solved analytically.

This paper is organized as follows. In Section 2, we propose an unconditionally stable second-order hybrid numerical method for solving the AC equation. The numerical results showing the accuracy, efficiency, and stability of the proposed method are presented in Section 3. Next, in Sections 4 and 5, we present applications of the AC equation. Finally, conclusions are drawn in Section 6.

2. The proposed operator splitting algorithm

In this section, an unconditionally stable second-order hybrid numerical method is proposed for solving the AC equation. The unconditional stability means that arbitrarily large time steps can be used in the numerical algorithm. For simplicity, we shall discretize the AC equation in one-dimensional space, i.e., $\Omega = (a, b)$. Two- and three-dimensional discretizations are defined analogously. Let N be a positive even integer, $h = (b - a)/N$ be a uniform grid size, and $\Omega_h = \{x_i = (i - 0.5)h,\ 1 \le i \le N\}$ be the set of cell centers. Let c_i^n be the approximations of $c(x_i, n\Delta t)$, where $\Delta t = T/N_t$ is the time step, T is the final time, and N_t is the total number of time steps. The zero Neumann boundary condition, Eq. (2), is first implemented by requiring that for each n,

$$\nabla_h c^n_{\frac{1}{2}} = \nabla_h c^n_{N+\frac{1}{2}} = 0, \tag{9}$$

where the discrete differentiation operator is $\nabla_h c^n_{i+\frac{1}{2}} = (c^n_{i+1} - c^n_i)/h$. We then define a discrete Laplacian operator as $\Delta_h c_i = \left(\nabla_h c_{i+\frac{1}{2}} - \nabla_h c_{i-\frac{1}{2}}\right)/h$ and a discrete l_2 inner product as

$$\langle \mathbf{c}, \mathbf{d} \rangle_h = h \sum_{i=1}^{N} c_i d_i, \tag{10}$$

where $\mathbf{c} = (c_1, c_2, \ldots, c_N)$. We also define the discrete l_2 and maximum norms, respectively, as $\|\mathbf{c}\|_h = \sqrt{\langle \mathbf{c}, \mathbf{c} \rangle_h}$ and $\|\mathbf{c}\|_\infty = \max_{1 \le i \le N} |c_i|$. We propose the following operator splitting scheme, which is an unconditionally stable second-order accurate hybrid scheme:

$$\frac{c_i^* - c_i^n}{\Delta t} = \frac{1}{2}(\Delta_h c_i^* + \Delta_h c_i^n), \tag{11}$$

$$\frac{c_i^{n+1} - c_i^*}{\Delta t} = \frac{c_i^{n+1} - (c_i^{n+1})^3}{\epsilon^2}. \tag{12}$$

Eq. (11) is a Crank–Nicolson scheme for $c_t = \Delta c$ with an initial condition c^n. Using a von Neumann stability analysis [25], it can be seen that this scheme is unconditionally stable. The resulting implicit discrete system of equations can be solved by a fast solver such as a multigrid method [26,27]. Eq. (12) can be considered as an approximation of the equation

$$c_t = \frac{c - c^3}{\epsilon^2} \tag{13}$$

by an implicit Euler's method with the initial condition c^*. We can solve Eq. (13) analytically by the method of separation of variables [28]. The solution is given as follows:

$$c_i^{n+1} = \frac{c_i^* e^{\frac{\Delta t}{\epsilon^2}}}{\sqrt{1 + (c_i^*)^2 \left(e^{\frac{2\Delta t}{\epsilon^2}} - 1\right)}} = \frac{c_i^*}{\sqrt{e^{-\frac{2\Delta t}{\epsilon^2}} + (c_i^*)^2 \left(1 - e^{-\frac{2\Delta t}{\epsilon^2}}\right)}}. \tag{14}$$

The proposed operator splitting algorithm is shown schematically in Fig. 2.

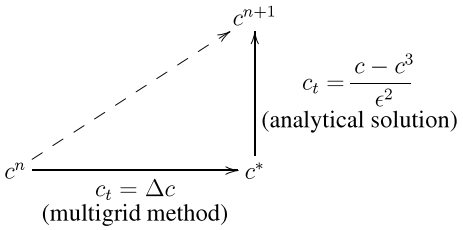

Fig. 2. A hybrid numerical method for the AC equation.

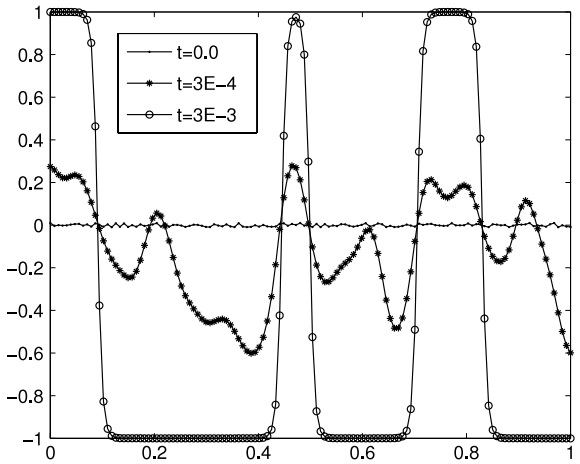

Fig. 3. The evolution of an initial random distribution of concentration, $c(x, 0) = 0.01\text{rand}(x)$. The concentration profile is shown at $t = 0$, 3E−4, and 3E−3.

Finally, the proposed scheme can be written as follows:

$$\frac{c_i^* - c_i^n}{\Delta t} = \frac{1}{2}(\Delta_h c_i^* + \Delta_h c_i^n) \quad \text{for } i = 1, \ldots, N \text{ and } n = 0, \ldots, N_t - 1 \tag{15}$$

$$c_i^{n+1} = \frac{c_i^*}{\sqrt{\mathrm{e}^{-\frac{2\Delta t}{\epsilon^2}} + (c_i^*)^2\left(1 - \mathrm{e}^{-\frac{2\Delta t}{\epsilon^2}}\right)}}. \tag{16}$$

3. Numerical experiments

In this section, the following numerical tests were performed: finding the relationship between the ϵ value and the width of the transition layer, traveling wave solutions, the convergence test, stability and accuracy tests, motion by the mean curvature, and the AC equation with a logarithmic free energy. From the results of these numerical tests, it was confirmed that the proposed scheme is second-order accurate in space and time and has unconditional stability.

3.1. The relationship between the ϵ value and the width of the transition layer

Across the interfacial regions, the concentration field varies from -0.9 to 0.9 over a distance of approximately $2\sqrt{2}\epsilon \tanh^{-1}(0.9)$. Therefore, if we want this value to be approximately m (> 0) grid points, the ϵ value needs to be taken as follows:

$$\epsilon_m = \frac{hm}{2\sqrt{2}\tanh^{-1}(0.9)}. \tag{17}$$

To confirm this, a simulation was run with the initial condition $c(x, 0) = 0.01$ rand(x) on the unit domain $\Omega = (0, 1)$ with $h = 1/128$, $\Delta t =$ E−5, and ϵ_4. Here, rand(x) is a random number between -1 and 1. In Fig. 3, the transition layer (from $c = -0.9$ to $c = 0.9$) is approximately four grid points at time $t =$ 3E−3 (circled line).

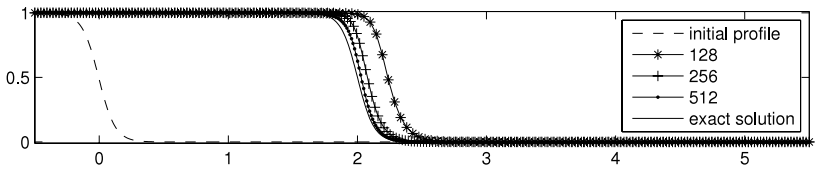

Fig. 4. Numerical traveling wave solutions with an initial profile (dashed line), $c(x,0) = \frac{1}{2}\left(1 - \tanh\frac{x}{2\sqrt{2}\epsilon}\right)$. The final time is $T = 2/s$. The analytic solution at T is a solid line. Lines with symbols, '$*$', '$+$', and '$\cdot$', represent 128, 256, and 512 grids, respectively.

Table 1
Convergence results in one dimension.

Case	128	Rate	256	Rate	512	Rate	1024
$\|\mathbf{e}^{N_t}\|_2$	3.444E−2	1.973	8.775E−3	1.962	2.252E−3	1.924	5.937E−4
$\|\mathbf{e}^{N_t}\|_\infty$	1.424E−1	1.969	3.637E−2	1.957	9.365E−3	1.915	2.483E−3

Table 2
Convergence results in two dimensions.

Case	128 × 128	Rate	256 × 256	Rate	512 × 512	Rate	1024 × 1024
$\|\mathbf{e}^{N_t}\|_2$	4.872E−2	1.973	1.241E−2	1.962	3.185E−3	1.929	8.367E−4
$\|\mathbf{e}^{N_t}\|_\infty$	1.425E−1	1.969	3.639E−2	1.960	9.351E−3	1.924	2.465E−3

3.2. Traveling wave solutions

Traveling wave solutions of Eq. (1) were obtained in the following form:

$$c(x,t) = \frac{1}{2}\left(1 - \tanh\frac{x - st}{2\sqrt{2}\epsilon}\right), \tag{18}$$

where $s = 3/(\sqrt{2}\epsilon)$ is the speed of the traveling wave [15]. In Fig. 4, we show the numerical traveling wave solutions (where the lines with symbols '$*$', '$+$', and '$\cdot$' represent 128, 256 and 512 grids, respectively) with an initial profile (dashed line), $c(x,0) = \frac{1}{2}\left(1 - \tanh\frac{x}{2\sqrt{2}\epsilon}\right)$, on a computational domain $\Omega = (-0.5, 5.5)$. The following are selected: final time $T = 2/s$, time step $\Delta t = T/16$, and $\epsilon = 0.0197$. The analytic final profile is $c(x,T) = \frac{1}{2}\left(1 - \tanh\frac{x-2}{2\sqrt{2}\epsilon}\right)$. The convergence of the results with the grid refinement is qualitatively evident.

3.3. The convergence test

The rate of convergence of the scheme is difficult to prove analytically. However, numerical experimentation suggests that the scheme is second-order accurate in space and time. A quantitative estimate of the rate of convergence was obtained by performing a number of simulations for the same initial profile on a set of increasingly finer space grids and time steps. The initial conditions are

$$c(x,0) = \frac{1}{2}\left(1 - \tanh\frac{x}{2\sqrt{2}\epsilon}\right), \tag{19}$$

$$c(x,y,0) = \frac{1}{2}\left(1 - \tanh\frac{x}{2\sqrt{2}\epsilon}\right), \quad \text{and} \tag{20}$$

$$c(x,y,z,0) = \frac{1}{2}\left(1 - \tanh\frac{x}{2\sqrt{2}\epsilon}\right) \tag{21}$$

for one-, two-, and three-dimensional tests, respectively. The numerical solutions with initial condition, Eqs. (19)–(21) were calculated on the computational domain $\Omega = (-0.5, 1.5)$, $\Omega = (-0.5, 1.5) \times (-0.5, 1.5)$, and $\Omega = (-0.5, 1.5) \times (-0.5/8, 1.5/8) \times (-0.5/8, 1.5/8)$, respectively. For one- and two-dimensional simulations, the parameters are $h = 2^{1-n}$, $\epsilon = 0.015$, and $s = 3/(\sqrt{2}\epsilon)$ for $n = 7, 8, 9,$ and 10. For each grid we integrate to time $T = 1/s$ with $\Delta t = h/(16s)$. Note that as we refine the space step we also refine the time step. The error of the numerical solution was defined as $\mathbf{e}^{N_t} = (e_1^{N_t}, e_2^{N_t}, \ldots, e_N^{N_t})$, where $e_i^{N_t} = c_i^{N_t} - c(x_i, T)$ for $i = 1, \ldots, N$. Tables 1–3 show the discrete l_2 and maximum norms of the errors and rates of convergence in one, two, and three dimensions, respectively. These results suggest that the scheme is indeed second-order accurate in space and time.

Table 3
Convergence results in three dimensions.

Case	64×8^2	Rate	128×16^2	Rate	256×32^2	Rate	512×64^2
$\|\mathbf{e}^{N_t}\|_2$	3.218E−2	1.902	8.612E−3	1.973	2.193E−3	1.969	5.601E−4
$\|\mathbf{e}^{N_t}\|_\infty$	4.909E−1	1.785	1.424E−1	1.969	3.638E−2	1.967	9.304E−3

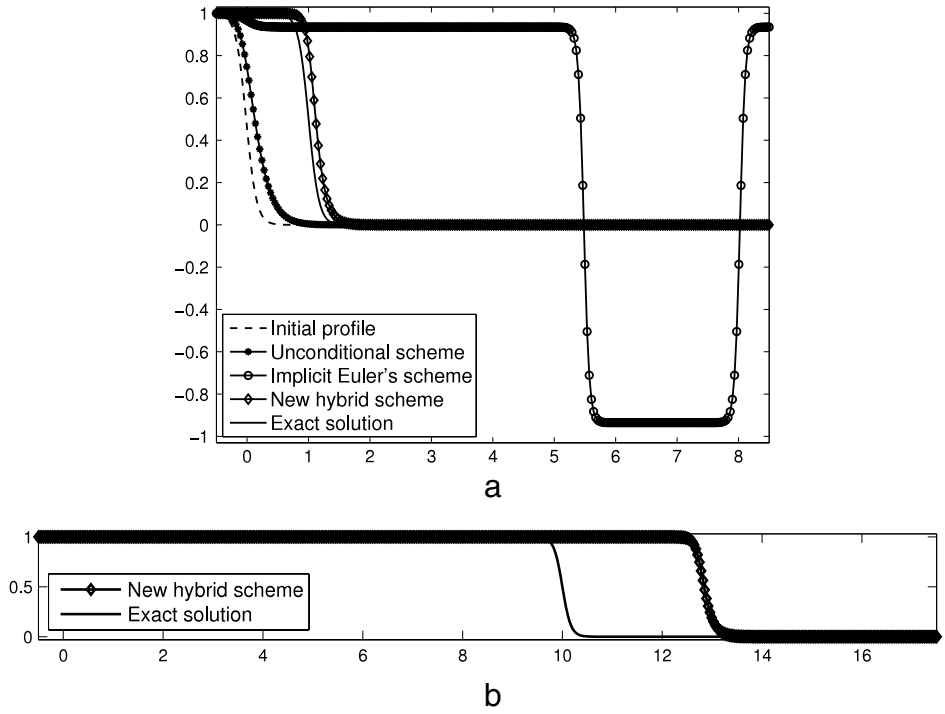

Fig. 5. (a) One-step evolutions with three different schemes with a time step $\Delta t = 1/s$. (b) A numerical solution with new hybrid scheme at $t = 10\Delta t$.

3.4. Stability and accuracy tests

The stability of the proposed numerical algorithm was compared with those for other methods. Fig. 5(a) shows one-step evolutions with three different schemes with a time step $\Delta t = 1/s$ and ϵ_7, on the computational domain $\Omega = (-0.5, 8.5)$ with a 256 grid. The dashed line is the initial configuration, $c(x, 0) = \frac{1}{2}\left(1 - \tanh\frac{x}{2\sqrt{2}\epsilon_7}\right)$, and the solid line is the exact solution, $c(x, \Delta t) = \frac{1}{2}\left(1 - \tanh\frac{x-1}{2\sqrt{2}\epsilon_7}\right)$, at time $t = \Delta t$. The lines denoted with the star, circle, and diamond symbols are the numerical solutions with the unconditional scheme, implicit Euler's scheme and new hybrid scheme, respectively. The result with the unconditional scheme traveled with the wrong speed, as was expected from the time step rescaling property, Eq. (8). In this case, the equivalent time step of the unconditional scheme is $\Delta t_{\text{equiv}} \approx 0.1115\Delta t$. The implicit Euler's scheme is unstable and reaches a wrong profile. The new hybrid scheme is closest to the exact solution and is stable with respect to a relatively large time step, $\Delta t = 1/s$. Fig. 5(b) shows a numerical solution with new hybrid scheme at $t = 10\Delta t$. We can see that the new hybrid scheme is stable with a long time evolution.

Next, we perform a numerical experiment with an example of spinodal decomposition of a binary mixture in order to demonstrate the unconditional stability of the scheme. In this simulation, the initial condition was random perturbation with the maximum amplitude 0.02:

$$c(x, y, 0) = 0.02\text{rand}(x, y). \tag{22}$$

A 64×64 mesh was used on the computational domain $\Omega = (0, 1) \times (0, 1)$ and different time steps, $\Delta t = 100$, $\Delta t = 10\,000$, and $\Delta t = 1000\,000$, were employed for the time integration. We took the simulation parameters $h = 1/64$ and ϵ_7. In Fig. 6, we display snapshots after ten time step iterations with three different time steps. These results suggest that the scheme is indeed unconditionally stable.

The effect of the equivalent time step was compared with the proposed numerical algorithm. Fig. 7 shows 200-step evolutions using two different schemes with a time step $\Delta t = \epsilon_7^2$, a 1024 grid and ϵ_7 on the computational domain $\Omega = (-0.5, 8.5)$. The dashed line is the initial configuration, $c(x, 0) = \frac{1}{2}\left(1 - \tanh\frac{x}{2\sqrt{2}\epsilon_7}\right)$, and the solid line is the exact

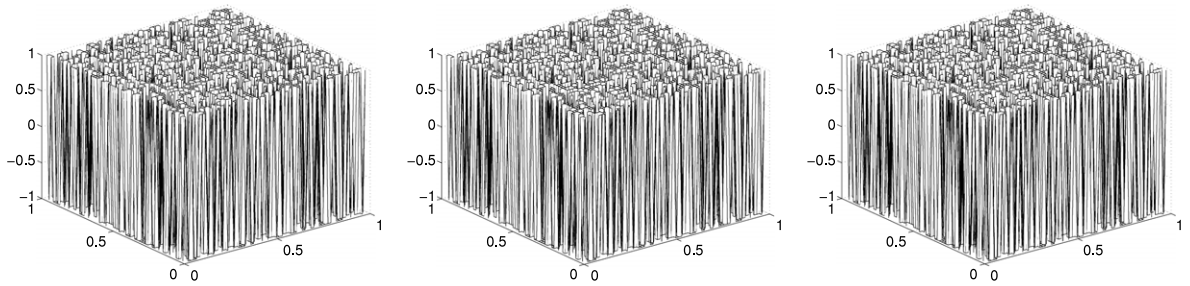

(a) $\Delta t = 100$. (b) $\Delta t = 10\,000$. (c) $\Delta t = 1000\,000$.

Fig. 6. Snapshots after ten time step iterations with three different time steps. The time steps are shown below each figure.

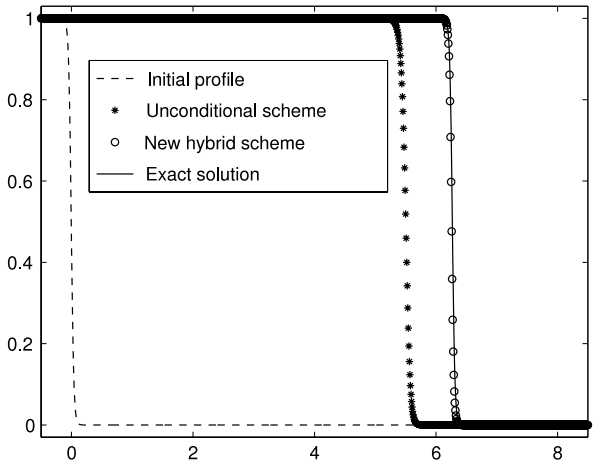

Fig. 7. The comparison with equivalent unconditional scheme with $\Delta t = \epsilon_7^2$ at time $t = 200\Delta t$.

solution calculated using Eq. (18) at time $t = 200\Delta t$. The results denoted with the star and circle are the numerical solutions with the unconditional scheme (Eq. (5)) and the new hybrid scheme, respectively. The result shows that while the numerical solution with the new hybrid scheme is close to the exact solution, the one with the unconditional scheme is far from the exact solution since the equivalent time step is $\Delta t_{\text{equiv}} = \Delta t\epsilon_7^2/(\Delta t + \epsilon_7^2) = 0.5\Delta t$.

3.5. Mean curvature flow

Numerical simulations of surfaces evolving according to their mean curvature are presented. Eq. (1) can be rewritten in the following form:

$$c_t = \frac{c - c^3}{\epsilon^2} + \Delta c. \tag{23}$$

It was formally shown that, as $\epsilon \to 0$, the zero level set of c, which is denoted by $\Gamma_t^\epsilon := \{\mathbf{x} \in \Omega : c(\mathbf{x}, t) = 0\}$, approaches a surface Γ_t that evolves according to the geometric law

$$V = -\kappa = -\left(\frac{1}{R_1} + \frac{1}{R_2}\right), \tag{24}$$

where V is the normal velocity of the surface, Γ_t, at each point, κ is its mean curvature, and R_1 and R_2 are the principal radii of curvatures at the point of the surface [1,29,30]. In d dimensions, with the same radii of curvature, Eq. (24) becomes

$$V = \frac{1 - d}{R}. \tag{25}$$

If the initial radius of the circular region is set to R_0 and the radius at time t is denoted as $R(t)$, then Eq. (25) becomes $\mathrm{d}R(t)/\mathrm{d}t = (1 - d)/R(t)$. Its solution is given as follows:

$$R(t) = \sqrt{R_0^2 + 2(1 - d)t}. \tag{26}$$

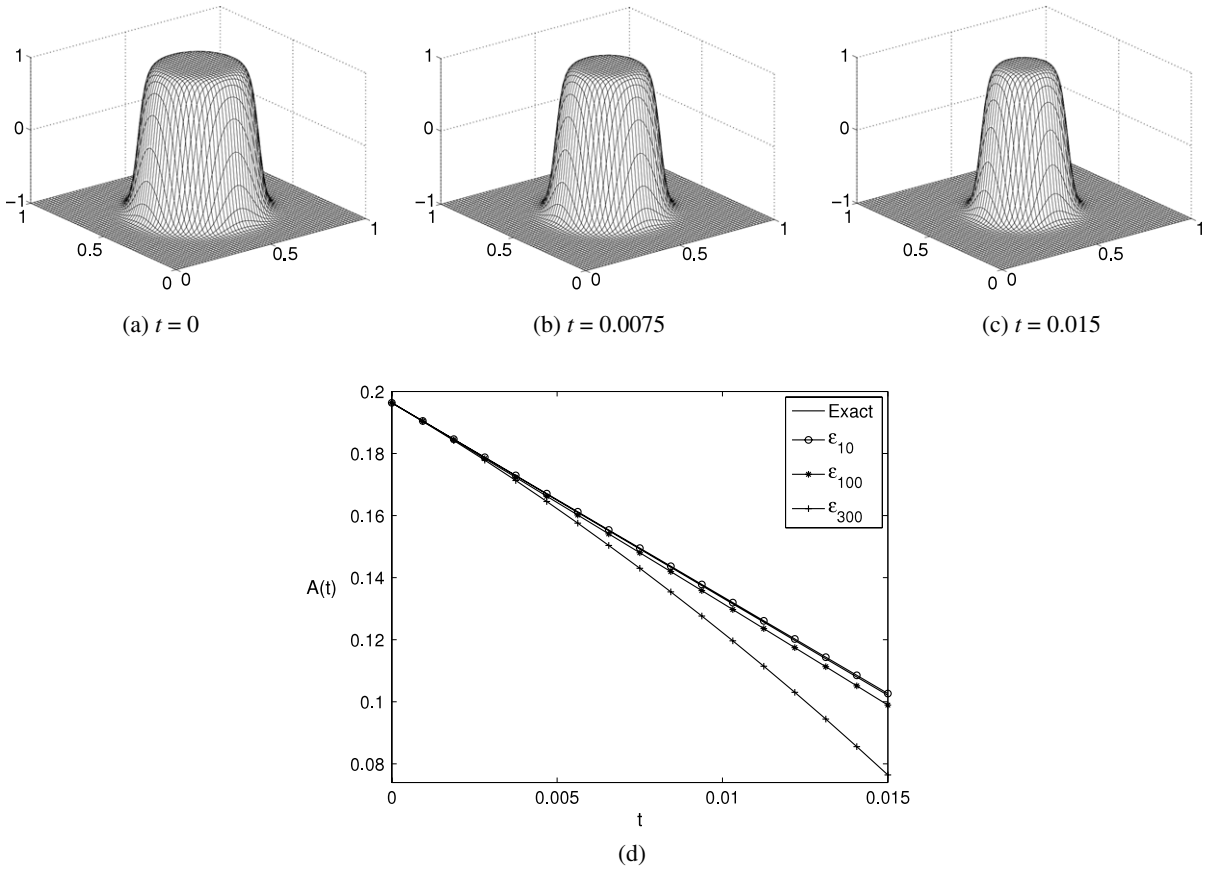

(a) $t = 0$ (b) $t = 0.0075$ (c) $t = 0.015$

(d)

Fig. 8. (a)–(c) show the evolution of the initial concentration $c(x, y, 0)$ given by Eq. (28). The times are shown below each figure. (d) illustrates evolution of the radius with three different ϵ. Lines with the '+', '∗', and '∘' symbols denote ϵ_{300}, ϵ_{100}, and ϵ_{10}, respectively.

Hence the analytic area $A(t)$ at time t is

$$A(t) = \pi(R_0^2 + 2(1 - d)t). \tag{27}$$

First, a two-dimensional test was performed with the following initial condition:

$$c(x, y, 0) = \tanh \frac{0.25 - \sqrt{(x - 0.5)^2 + (y - 0.5)^2}}{\sqrt{2}\epsilon} \tag{28}$$

on the computational domain $\Omega = (0, 1) \times (0, 1)$ with a 512×512 mesh and a time step $\Delta t = 0.0015h$. Fig. 8(a)–(c) show the evolution of the initial concentration $c(x, y, 0)$ given by Eq. (28). The times are shown below each figure. Fig. 8(d) shows that as the ϵ size decreases from ϵ_{300} ('+') to ϵ_{100} ('∗') and ϵ_{10} ('∘'), the numerical area $A(t)$ of the circle, with time, approaches the asymptotic value (solid line) given by Eq. (26).

Next, a three-dimensional test was performed with the following initial condition:

$$c(x, y, z, 0) = \tanh \frac{0.4 - \sqrt{(x - 0.5)^2 + (y - 0.5)^2 + (z - 0.5)^2}}{\sqrt{2}\epsilon} \tag{29}$$

on the computational domain $\Omega = (0, 1) \times (0, 1) \times (0, 1)$ with a $256 \times 256 \times 256$ mesh and a time step $\Delta t = 7\text{E}{-6}$. Fig. 9 presents snapshots of the zero isosurface of the solution in three-dimensional space. The times are shown below each figure. At time $t = 0.0175$, the numerical radii of the sphere are 0.2999 (ϵ_{20}), 0.2991 (ϵ_{40}), and 0.2990 (ϵ_{60}), respectively. The analytic radius from Eq. (26) is 0.3. From these two- and three-dimensional numerical tests, it was confirmed that $\Gamma_t^\epsilon \to \Gamma_t$ as $\epsilon \to 0$.

Fig. 10 shows the evolution of a star-shaped interface in a curvature-driven flow on the computational domain $\Omega = (0, 1) \times (0, 1)$ with a 128×128 mesh and $\Delta t = 5\text{E}{-5}$. The initial configuration is defined as follows:

$$c(x, y, 0) = \tanh \frac{0.25 + 0.1\cos(7\theta) - \sqrt{(x - 0.5)^2 + (y - 0.5)^2}}{\sqrt{2}\epsilon_4}, \tag{30}$$

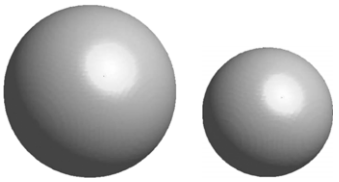

(a) $t = 0$. (b) $t = 0.0175$.

Fig. 9. (a) and (b) are initial and final isosurfaces.

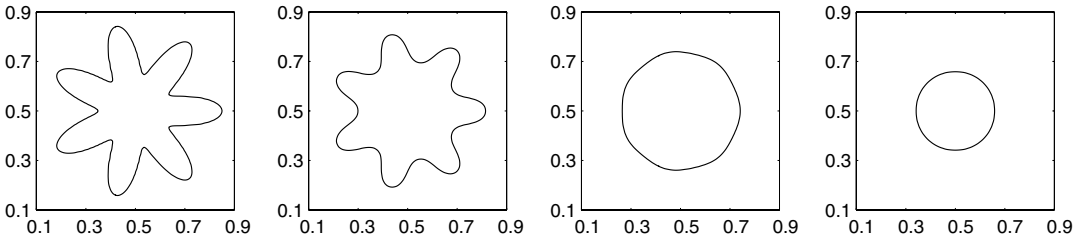

(a) $t = 0$. (b) $t = 0.001$. (c) $t = 0.005$. (d) $t = 0.020$.

Fig. 10. Evolution of a star-shaped interface in a curvature-driven flow. The tips of the star move inward, while the gaps between the tips move outward.

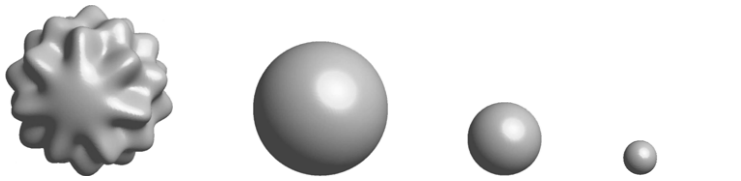

(a) $t = 0$. (b) $t = 0.003$. (c) $t = 0.012$. (d) $t = 0.015$.

Fig. 11. Evolution of a sphere perturbed with a spherical harmonic in a curvature-driven flow.

where

$$\theta = \begin{cases} \tan^{-1}\left(\dfrac{y-0.5}{x-0.5}\right) & \text{if } x > 0.5 \\ \pi + \tan^{-1}\left(\dfrac{y-0.5}{x-0.5}\right) & \text{otherwise.} \end{cases} \tag{31}$$

The tips of the star move inward, while the gaps between the tips move outward. Once the form deforms to a circular shape, the radius of the circle shrinks with increasing speed.

Fig. 11 shows the evolution of a sphere perturbed with a spherical harmonic in curvature-driven flow on the computational domain $\Omega = (0, 1) \times (0, 1) \times (0, 1)$ with a $256 \times 256 \times 256$ mesh and $\Delta t = \text{E}{-}5$. The initial configuration is defined as follows:

$$c(x, y, z, 0) = \tanh \frac{0.25 + 0.1Y_{10,7}(\theta, \phi) - r}{\sqrt{2}\epsilon_8}, \tag{32}$$

where $r = \sqrt{(x-0.5)^2 + (y-0.5)^2 + (z-0.5)^2}$, $Y_{10,7}(\theta, \phi)$ is a spherical harmonic [31],

$$\theta = \begin{cases} \tan^{-1}\left(\dfrac{y-0.5}{x-0.5}\right) & \text{if } x > 0.5 \\ \pi + \tan^{-1}\left(\dfrac{y-0.5}{x-0.5}\right) & \text{otherwise} \end{cases} \tag{33}$$

is a polar angle, and $\phi = \cos^{-1}\left(\frac{z-0.5}{r}\right)$ is the azimuthal angle. As in the two-dimensional case, once the form deforms to a spherical shape, the radius of the sphere shrinks with increasing speed.

Fig. 12 shows the temporal evolution of the two-dimensional dumbbell shape. The initial configuration is given by a dumbbell where the inner strip is centered on $y = 0.5$, and has a width of 0.2, and the circles at either end of the strip have centers at (0.3, 0.5), (1.7, 0.5) with a radius of 0.2. The computation is performed on a 512×256 mesh with $h = 1/256$, ϵ_{15}, $\Delta t = 8\text{E}{-}5$, and $T = 0.072$. The thicker line represents the initial configuration and the succeeding contour lines are incremented by the time interval 4.8E−3.

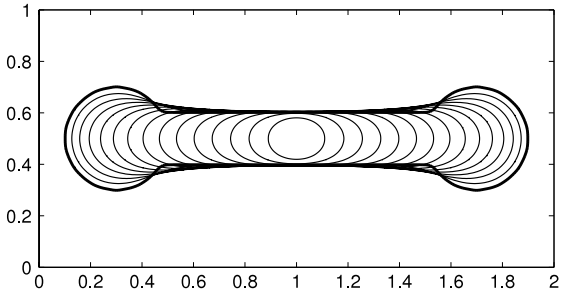

Fig. 12. Temporal evolution of the two-dimensional dumbbell shape. The computation was performed on a 512 × 256 mesh with $h = 1/256$, ϵ_{15}, $\Delta t = 8\text{E}{-5}$, and $T = 0.072$. The thicker line represents the initial configuration and the succeeding contour lines are increased by the time interval 4.8E−3.

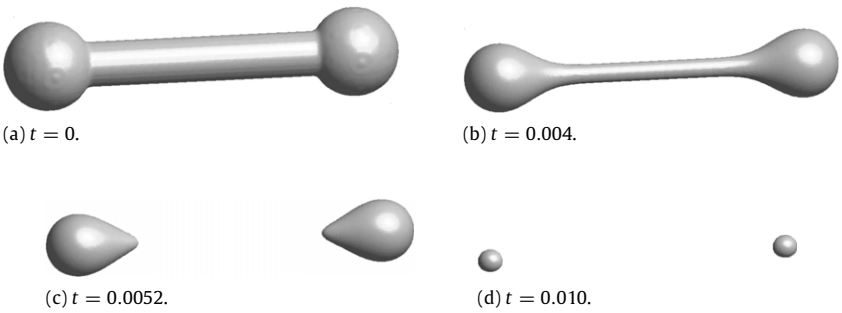

Fig. 13. Temporal evolution by the mean curvature of the three-dimensional dumbbell shape. (a) The initial surface. The times are shown below each figure. The computation was performed on a 256 × 128 × 128 grid.

Fig. 13 shows the temporal evolution of a three-dimensional dumbbell shape. The initial configuration is given by a dumbbell where the inner cylinder, which is centered on $(x, 0.5, 0.5)$, has a radius of 0.1, and the spheres at either end of the cylinder have centers at $(0.3, 0.5, 0.5)$, $(1.7, 0.5, 0.5)$ with a radius 0.2. The computation was carried out on a 256 × 128 × 128 mesh with $h = 1/128$, ϵ_8, and $\Delta t = 4\text{E}{-5}$. Initially the radius of the handle was much smaller than that of the spheres on the end. Therefore, the handle was expected to shrink at a faster rate, so the handle would pinch off after some time. The handle pinches off at approximately $t = 0.005$, and the two spheres disappear at approximately $t = 0.0106$.

Fig. 14 shows the evolution of the double circles on the computational domain $\Omega = (0, 1) \times (0, 1)$ with a 128 × 128 mesh and $\Delta t = 6\text{E}{-5}$. The initial configuration is defined as follows:

$$c(x, y, 0) = \tanh \frac{0.4 - \sqrt{(x-0.5)^2 + (y-0.5)^2}}{\sqrt{2}\epsilon} - \tanh \frac{0.3 - \sqrt{(x-0.5)^2 + (y-0.5)^2}}{\sqrt{2}\epsilon} - 1. \tag{34}$$

The smaller circle has a larger curvature, and shrinks faster than the larger circle. After the smaller circle disappears, the larger one also decreases in size.

Fig. 15(a) shows the evolution of the torus in a curvature-driven flow on the computational domain $\Omega = (0, 2) \times (0, 2) \times (0, 1)$ with a 256 × 256 × 128 mesh, $\Delta t = 4\text{E}{-5}$, and ϵ_8. Fig. 15(b) and (c) show the horizontal and vertical sections of the torus, respectively. Unlike for the two-dimensional case, the inner circle increases in size because the mean curvature drives the motion into the inside of the torus. This is a three-dimensional phenomenon.

3.6. The Allen–Cahn equation with a logarithmic free energy

Our proposed method can be applied to a class of potentials $F(c)$. For example, let us consider the logarithmic free energy, i.e., $F(c) = \frac{\theta}{2}[(1+c)\ln(1+c) + (1-c)\ln(1-c)] - \frac{\theta_c}{2}c^2$, where θ and θ_c are positive constants with $\theta < \theta_c$. Fig. 16 shows the logarithmic free energy $F(c)$ with $\theta = 1.0$ and $\theta_c = 1.2$.

In this case, we propose the following operator splitting scheme:

$$\frac{c_i^* - c_i^n}{\Delta t} = \frac{1}{2}(\Delta_h c_i^* + \Delta_h c_i^n), \tag{35}$$

$$\frac{c_i^{n+1} - c_i^*}{\Delta t} = -\frac{1}{2\epsilon^2}(F'(c^{n+1}) + F'(c^*)). \tag{36}$$

Since a closed-form solution is not available for $c_t = -F'(c)/\epsilon^2$ with a logarithmic free energy, we apply Newton's method [32] to solve Eq. (36). It turns out that Newton's algorithm typically requires only one or two iterations to achieve acceptable accuracy.

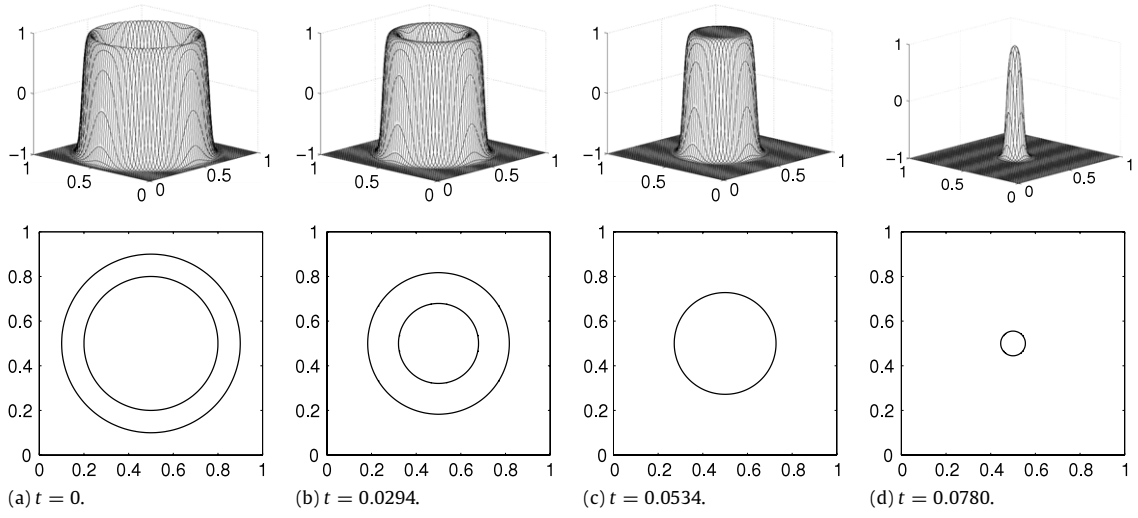

Fig. 14. Evolution of the double circles in a curvature-driven flow on the domain $\Omega = (0, 1) \times (0, 1)$ with a 128×128 mesh, $\Delta t = 6\text{E}{-5}$, and ϵ_8.

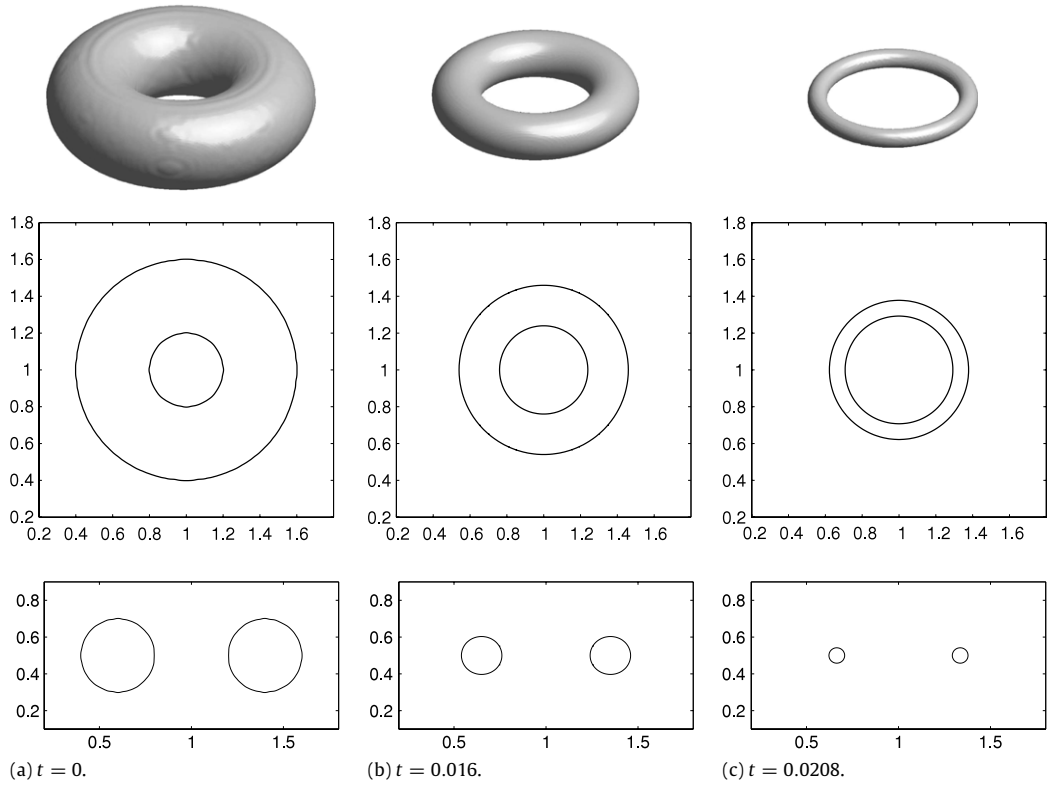

Fig. 15. Evolution of the torus in curvature-driven flow on the domain $\Omega = (0, 2) \times (0, 2) \times (0, 1)$ with a $256 \times 256 \times 128$ mesh, $\Delta t = 4\text{E}{-5}$, and ϵ_8.

As a test problem, we consider spinodal decomposition of a binary mixture. The initial condition was random perturbation with the maximum amplitude 0.1:

$$c(x, y, 0) = 0.1\text{rand}(x, y) \tag{37}$$

on the computational domain $\Omega = (0, 1) \times (0, 1)$. In this test, a 64×64 mesh and a time step $\Delta t = 5\text{E}{-5}$ were used. We took the simulation parameters $h = 1/64$, $\epsilon = 0.0075$, $\theta = 1.0$, and $\theta_c = 1.2$. In Fig. 17, we display the evolution of the phase field at different times. From the results it can be seen that our proposed scheme is applicable to the AC equation with potentials other than $F'(c) = c^3 - c$.

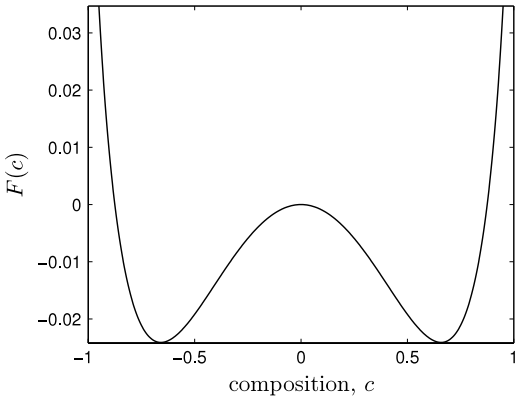

Fig. 16. A logarithmic free energy, $F(c) = \frac{\theta}{2}[(1+c)\ln(1+c) + (1-c)\ln(1-c)] - \frac{\theta_c}{2}c^2$, with $\theta = 1.0$ and $\theta_c = 1.2$.

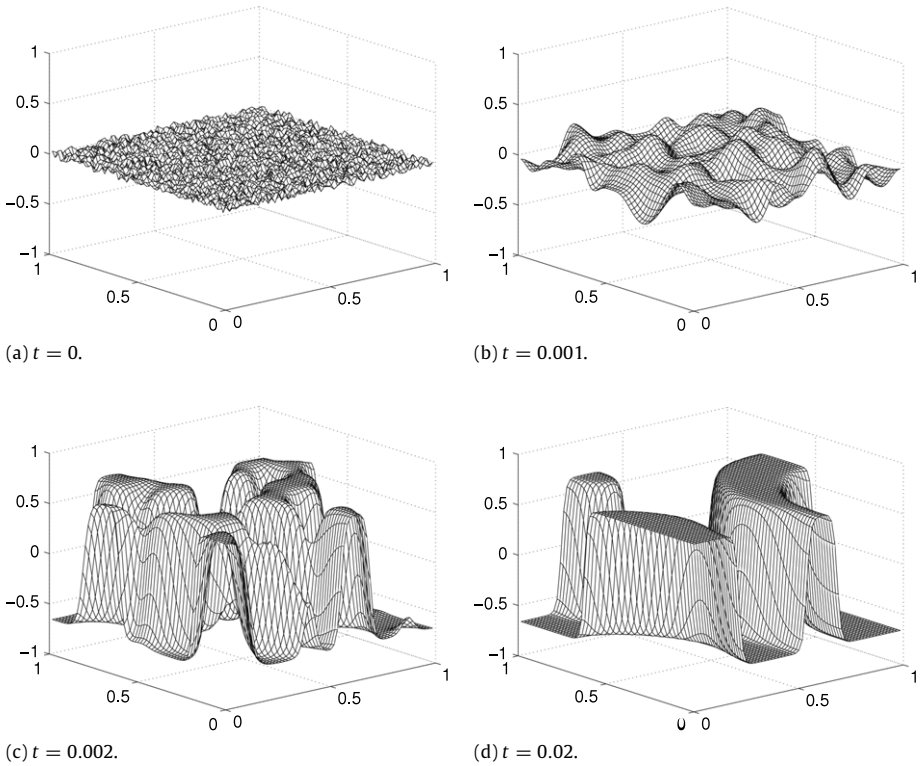

Fig. 17. The evolutions of the phase field at different times. The times are shown below each figure.

4. The application for crystal growth

Crystal growth is a classical example of a phase transformation from the liquid phase to the solid phase via heat transfer. The basic equations of the phase-field model are derivable from a single Lyapunov functional when expressed in the variational form [33]. We begin by rescaling the temperature field T, $U = c_p(T - T_M)/L$, where c_P is the specific heat at constant pressure, L is the latent heat of fusion, and T_M is the melting temperature. The order parameter is given as ϕ, where we define $\phi = 1$ in the solid phase and $\phi = -1$ in the liquid phase. The interface is defined by $\phi = 0$. We rescale time throughout by τ_0, a time characterizing atomic movement in the interface. Length is rescaled by w_0, a length characterizing the liquid–solid interface. With these definitions, the model is written as

$$\begin{aligned}\epsilon^2(\phi)\frac{\partial\phi}{\partial t} &= \nabla\cdot(\epsilon^2(\phi)\nabla\phi) + [\phi - \lambda U(1-\phi^2)](1-\phi^2) \\ &\quad + \left(|\nabla\phi|^2\epsilon(\phi)\frac{\partial\epsilon(\phi)}{\partial\phi_x}\right)_x + \left(|\nabla\phi|^2\epsilon(\phi)\frac{\partial\epsilon(\phi)}{\partial\phi_y}\right)_y + \left(|\nabla\phi|^2\epsilon(\phi)\frac{\partial\epsilon(\phi)}{\partial\phi_z}\right)_z, \end{aligned} \tag{38}$$

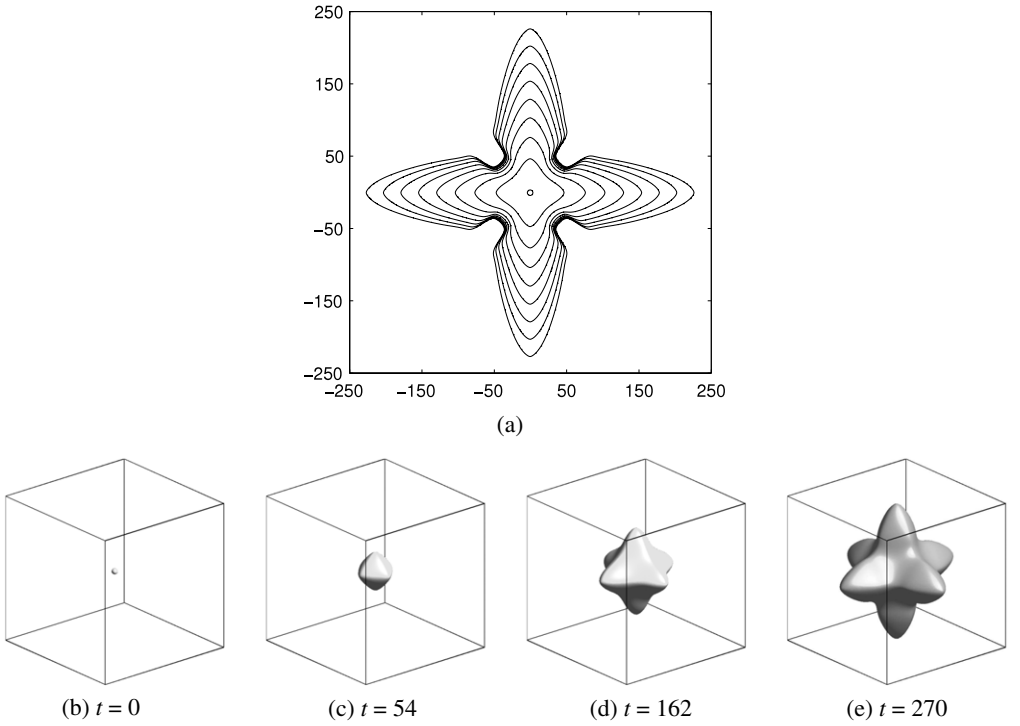

(a) (b) $t = 0$ (c) $t = 54$ (d) $t = 162$ (e) $t = 270$

Fig. 18. (a) Sequence of interface shapes for the initial solid in two dimensions with the total time $t = 1800$. ((b)–(e)) Sequence of interface 3D shapes in three dimensions.

$$\frac{\partial U}{\partial t} = D\Delta U + \frac{1}{2}\frac{\partial \phi}{\partial t}, \tag{39}$$

where $D = \alpha\tau_0/w_0^2$ and α is the thermal diffusivity. λ is the dimensionless coupling parameter. The anisotropic function $\epsilon(\phi)$ in Eq. (38) is defined for the fourfold symmetry as

$$\epsilon(\phi) = (1 - 3\bar{\epsilon})\left(1 + \frac{4\bar{\epsilon}}{1 - 3\bar{\epsilon}}\frac{\phi_x^4 + \phi_y^4 + \phi_z^4}{|\nabla\phi|^4}\right), \tag{40}$$

where $\bar{\epsilon}$ is a parameter for the interface energy anisotropy. With the addition of this unconditionally stable hybrid method, for simplicity of exposition, we shall discretize the crystal growth simulation in two dimensions as the following operator splitting numerical algorithm:

$$\epsilon^2(\phi^n)\frac{\phi^{n+1,1} - \phi^n}{\Delta t} = 2\epsilon(\phi^n)\nabla\epsilon(\phi^n)\cdot\nabla\phi^n + \left(|\nabla\phi|^2\epsilon(\phi)\frac{\partial\epsilon(\phi)}{\partial\phi_x}\right)_x^n + \left(|\nabla\phi|^2\epsilon(\phi)\frac{\partial\epsilon(\phi)}{\partial\phi_y}\right)_y^n, \tag{41}$$

$$\epsilon^2(\phi^n)\frac{\phi^{n+1,2} - \phi^{n+1,1}}{\Delta t} = -4\lambda U^n F(\phi^{n+1,1}), \tag{42}$$

$$\epsilon^2(\phi^n)\frac{\phi^{n+1,3} - \phi^{n+1,2}}{\Delta t} = \epsilon^2(\phi^n)\Delta\phi^{n+1,3}, \tag{43}$$

$$\epsilon^2(\phi^n)\frac{\phi^{n+1} - \phi^{n+1,3}}{\Delta t} = -F'(\phi^{n+1}), \tag{44}$$

$$\frac{U^{n+1} - U^n}{\Delta t} = D\Delta_d U^{n+1} + \frac{\phi^{n+1} - \phi^n}{2\Delta t}, \tag{45}$$

where $F(\phi) = 0.25(\phi^2 - 1)^2$ and $F'(\phi) = \phi(\phi^2 - 1)$. With this updated value of ϕ^{n+1}, we calculate U^{n+1} using Eq. (45).

In our numerical experiments, the initial interfaces in two and three dimensions are specified, respectively, by

$$\phi(x, y) = \tanh\left(\frac{R_n - \sqrt{x^2 + y^2}}{\sqrt{2}}\right),$$

$$U(x,y)=\begin{cases}0 & \text{if } \phi>0\\ \Delta & \text{else}\end{cases} \tag{46}$$

$$\phi(x,y,z)=\tanh\left(\frac{R_n-\sqrt{x^2+y^2+z^2}}{\sqrt{2}}\right),$$

$$U(x,y,z)=\begin{cases}0 & \text{if } \phi>0\\ \Delta & \text{else.}\end{cases} \tag{47}$$

And the following parameters are used: time step $\Delta t=0.15$, uniform grid size $h=0.78$, $R_n=14d_0$, $d_0=0.277$, $D=2$, $\lambda=3.191$, $\bar{\epsilon}=0.05$, and $\Delta=-0.55$. In Fig. 18, we show the temporal evolutions of the crystal growth in two and three dimensions.

5. The application for image segmentation

The segmentation of structure from images is an important first step for object recognition, interpretation and image inpainting. One of the approaches is a variational model, in which the image segmentation is obtained as the minimizer of the piecewise constant Mumford–Shah functional. A phase-field approximation for minimizing the Mumford–Shah functional, by using AC equation to replace the length of the segmenting curve C, is given by the following gradient descent flow equation:

$$\phi_t=-\frac{F'(\phi)}{\varepsilon^2}+\Delta\phi-\lambda[(1+\phi)(f_0-c_1)^2-(1-\phi)(f_0-c_2)^2] \tag{48}$$

$$\phi(\mathbf{x})\begin{cases}>0 & \text{if } \mathbf{x}\in \text{ inside } C,\\ =0 & \text{if } \mathbf{x}\in C,\\ <0 & \text{if } \mathbf{x}\in \text{ outside } C\end{cases} \tag{49}$$

where $F'(\phi)=\phi(\phi^2-1)$, λ is a nonnegative parameter and f_0 is the given image. Also c_1 and c_2 are the averages of f_0 in the regions $(\phi\geq 0)$ and $(\phi<0)$, respectively:

$$c_1=\frac{\int_\Omega f_0(\mathbf{x})(1+\phi(\mathbf{x}))d\mathbf{x}}{\int_\Omega(1+\phi(\mathbf{x}))d\mathbf{x}} \quad\text{and}\quad c_2=\frac{\int_\Omega f_0(\mathbf{x})(1-\phi(\mathbf{x}))d\mathbf{x}}{\int_\Omega(1-\phi(\mathbf{x}))d\mathbf{x}}. \tag{50}$$

Then using an unconditionally stable hybrid method, the following operator splitting numerical algorithm is proposed:

$$\frac{\phi^{n+1,1}-\phi^n}{\Delta t}=-\lambda[(1+\phi^{n+1,1})(f_0-c_1)^2-(1-\phi^{n+1,1})(f_0-c_2)^2], \tag{51}$$

$$\frac{\phi^{n+1,2}-\phi^{n+1,1}}{\Delta t}=\Delta_d\phi^{n+1,2}, \tag{52}$$

$$\frac{\phi^{n+1}-\phi^{n+1,2}}{\Delta t}=-\frac{F'(\phi^{n+1})}{\epsilon^2}. \tag{53}$$

In our numerical experiments, we normalize the given image f as $f_0=\frac{f-f_{\min}}{f_{\max}-f_{\min}}$, where $f_{\max}$ and $f_{\min}$ are the maximum and the minimum values of the given image, respectively. Then $f_0\in[0,1]$. We simply used $\phi=2f_0-1$ as the initial condition. In Fig. 19(a) we show the original image of Europe night light. And in Fig. 19(b)–(d) we show the segmentation of the initial image with different iterations. The computational domain is $\Omega=(0,1)\times(0,1)$ with a 256×256 mesh. The interface parameter ϵ_{600}, time step $\Delta t=1.25\text{E}{-4}$, and $\lambda=7.5\text{E}{+4}$ are used. We show that our proposed scheme can also be used to solve the image segmentation problem.

6. Conclusions

As Eyre noticed, the explicit Euler's scheme for the CH equation is not gradient stable and the stable time steps are severely restricted. The implicit Euler's scheme is conditionally gradient stable and it suffers from the uniqueness problem for solutions with large time steps. It turns out that the allowed time step sizes are just less than twice the explicit Euler's step. The Crank–Nicolson scheme also suffers from the solvability restriction. The semi-implicit Euler's scheme is much better than the explicit Euler's scheme, but still not gradient stable [22]. Eyre's scheme also has the equivalent time step limitation. In this paper, an unconditionally stable second-order hybrid numerical method was developed for solving the AC equation. The proposed method was based on operator splitting techniques. The linear equation was solved using a Crank–Nicolson scheme and the nonlinear equation was then solved analytically. A variety of numerical experiments were presented to confirm the accuracy, efficiency, and stability of the proposed method. In particular, the scheme was shown to be unconditionally stable and second-order accurate in both time and space.

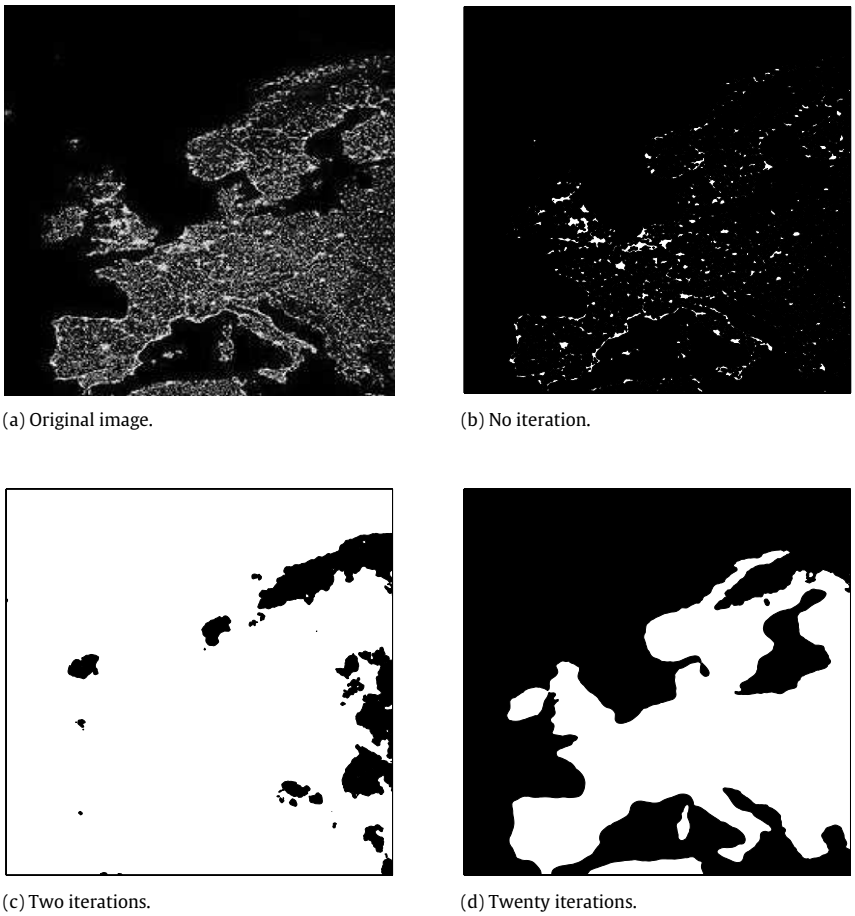

(a) Original image. (b) No iteration.

(c) Two iterations. (d) Twenty iterations.

Fig. 19. Europe night light. (a) Original image, (b) contour of the initial image, (c) two iterations, and (d) twenty iterations.

Acknowledgements

This research was supported by the Basic Science Research Program through the National Research Foundation of Korea (NRF) funded by the Ministry of Education, Science and Technology (No. 2009-0074248). The authors thank the reviewers for their constructive and valuable comments regarding the revision of this article.

References

[1] S.M. Allen, J.W. Cahn, A microscopic theory for antiphase boundary motion and its application to antiphase domain coarsening, Acta Metall. 27 (1979) 1085–1095.
[2] E.V.L. Melloa, Otton Teixeira da Silveira Filho, Numerical study of the Cahn–Hilliard equation in one, two and three dimensions, Physica A 347 (2005) 429–443.
[3] C. Cowan, The Cahn–Hilliard equation as a gradient flow, Simon Fraser University, Canada, 2005.
[4] M. Beneš, V. Chalupecký, K. Mikula, Geometrical image segmentation by the Allen–Cahn equation, Appl. Numer. Math. 51 (2004) 187–205.
[5] J.A. Dobrosotskaya, A.L. Bertozzi, A Wavelet–Laplace variational technique for image deconvolution and inpainting, IEEE Trans. Image Process. 17 (2008) 657–663.
[6] M. Beneš, K. Mikula, Simulation of anisotropic motion by mean curvature—comparison of phase field and sharp interface approaches, Acta Math. Univ. Comenian. 67 (1998) 17–42.
[7] L.C. Evans, H.M. Soner, P.E. Souganidis, Phase transitions and generalized motion by mean curvature, Comm. Pure Appl. Math. 45 (1992) 1097–1123.
[8] X. Feng, A. Prohl, Numerical analysis of the Allen–Cahn equation and approximation for mean curvature flows, Numer. Math. 94 (2003) 33–65.
[9] T. Ilmanen, Convergence of the Allen–Cahn equation to Brakke's motion by mean curvature, J. Differential Geom. 38 (1993) 417–461.
[10] M. Katsoulakis, G.T. Kossioris, F. Reitich, Generalized motion by mean curvature with Neumann conditions and the Allen–Cahn model for phase transitions, J. Geom. Anal. 5 (1995) 255–279.
[11] T. Ohtsuka, Motion of interfaces by an Allen–Cahn type equation with multiple-well potentials, Asymptot. Anal. 56 (2008) 87–123.
[12] X. Yang, J.J. Feng, C. Liu, J. Shen, Numerical simulations of jet pinching-off and drop formation using an energetic variational phase-field method, J. Comput. Phys. 218 (2006) 417–428.
[13] M. Cheng, J.A. Warren, An efficient algorithm for solving the phase field crystal model, J. Comput. Phys. 227 (2008) 6241–6248.
[14] A.A. Wheeler, W.J. Boettinger, G.B. McFadden, Phase-field model for isothermal phase transitions in binary alloys, Phys. Rev. A 45 (1992) 7424–7439.
[15] J.-W. Choi, H.G. Lee, D. Jeong, J. Kim, An unconditionally gradient stable numerical method for solving the Allen–Cahn equation, Physica A 388 (2009) 1791–1803.

[16] X. Feng, H.-J. Wu, A posteriori error estimates and an adaptive finite element method for the Allen–Cahn equation and the mean curvature flow, J. Sci. Comput. 24 (2005) 121–146.
[17] W.M. Feng, P. Yu, S.Y. Hu, Z.K. Liu, Q. Du, L.Q. Chen, Spectral implementation of an adaptive moving mesh method for phase-field equations, J. Comput. Phys. 220 (2006) 498–510.
[18] D.F. Martin, P. Colella, M. Anghel, F.L. Alexander, Adaptive mesh refinement for multiscale nonequilibrium physics, Comput. Sci. Eng. 7 (2005) 24–31.
[19] Q. Du, W. Zhu, Stability analysis and applications of the exponential time differencing schemes, J. Comput. Math. 22 (2004) 200–209.
[20] S.M. Cox, P.C. Matthews, Exponential time differencing for stiff systems, J. Comput. Phys. 176 (2002) 430–455.
[21] D.J. Eyre, Computational and Mathematical Models of Microstructural Evolution, The Materials Research Society, Warrendale, 1998.
[22] D.J. Eyre, http://www.math.utah.edu/~eyre/research/methods/stable.ps.
[23] M. Cheng, A.D. Rutenberg, Maximally fast coarsening algorithms, Phys. Rev. E 72 (2005) 055701(R).
[24] B.P. Vollmayr-Lee, A.D. Rutenberg, Fast and accurate coarsening simulation with an unconditionally stable time step, Phys. Rev. E 68 (2003) 066703.
[25] D.J. Duffy, Finite Difference Methods in Financial Engineering: A Partial Differential Equation Approach, Wiley Finance, Chichester, UK, 2006.
[26] W.L. Briggs, A Multigrid Tutorial, SIAM, Philadelphia, PA, 1987.
[27] U. Trottenberg, C. Oosterlee, A. Schüller, Multigrid, Academic Press, USA, 2001.
[28] A. Stuart, A.R. Humphries, Dynamical System and Numerical Analysis, Cambridge University Press, Cambridge, 1998.
[29] W. Bao, Approximation and comparison for motion by mean curvature with intersection points, Comput. Math. Appl. 46 (2003) 1211–1228.
[30] P.C. Fife, Dynamics of Internal Layers and Diffusive Interfaces, SIAM, Philadelphia, PA, 1988.
[31] V. Cristini, J. Lowengrub, Three-dimensional crystal growth—II: nonlinear simulation and control of the Mullins–Sekera instability, J. Cryst. Growth 266 (2004) 552–567.
[32] R.L. Burden, J.D. Faires, Numerical Analysis, Thomson, 2004.
[33] J.S. Langer, Directions in Condensed Matter, World Scientific, Singapore, 1986, p. 164.